Electronic Supplementary Material (ESI) for Journal of Materials Chemistry C.

Supporting Information

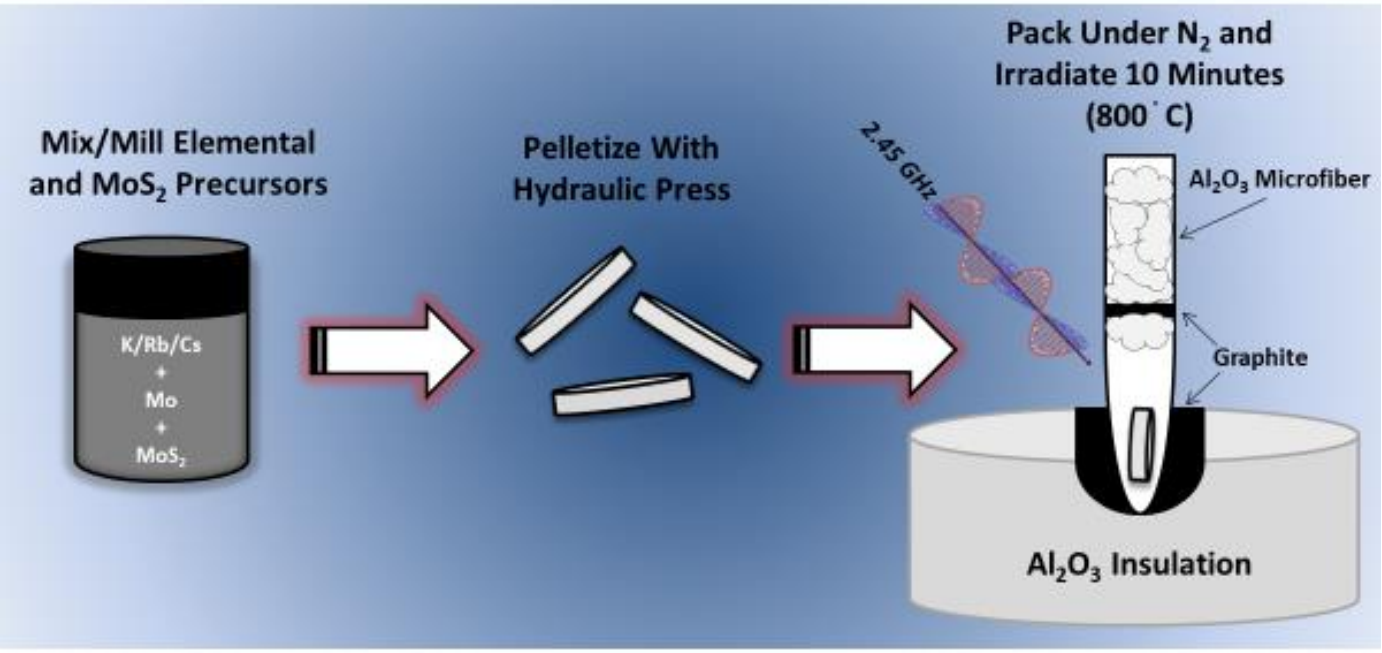

Figure S1. Schematic illustration of the synthetic method wherein the fused quartz reaction vessel is packed tightly with microfibrous Al_2O_3 and a layer of sacrificial graphite in order to isolate compressed pellets with $M_2Mo_6S_6$ stoichiometry under an inert atmosphere during heating. The entirety of the far-right figure is placed in a microwave chamber under continuous flow of Ar.

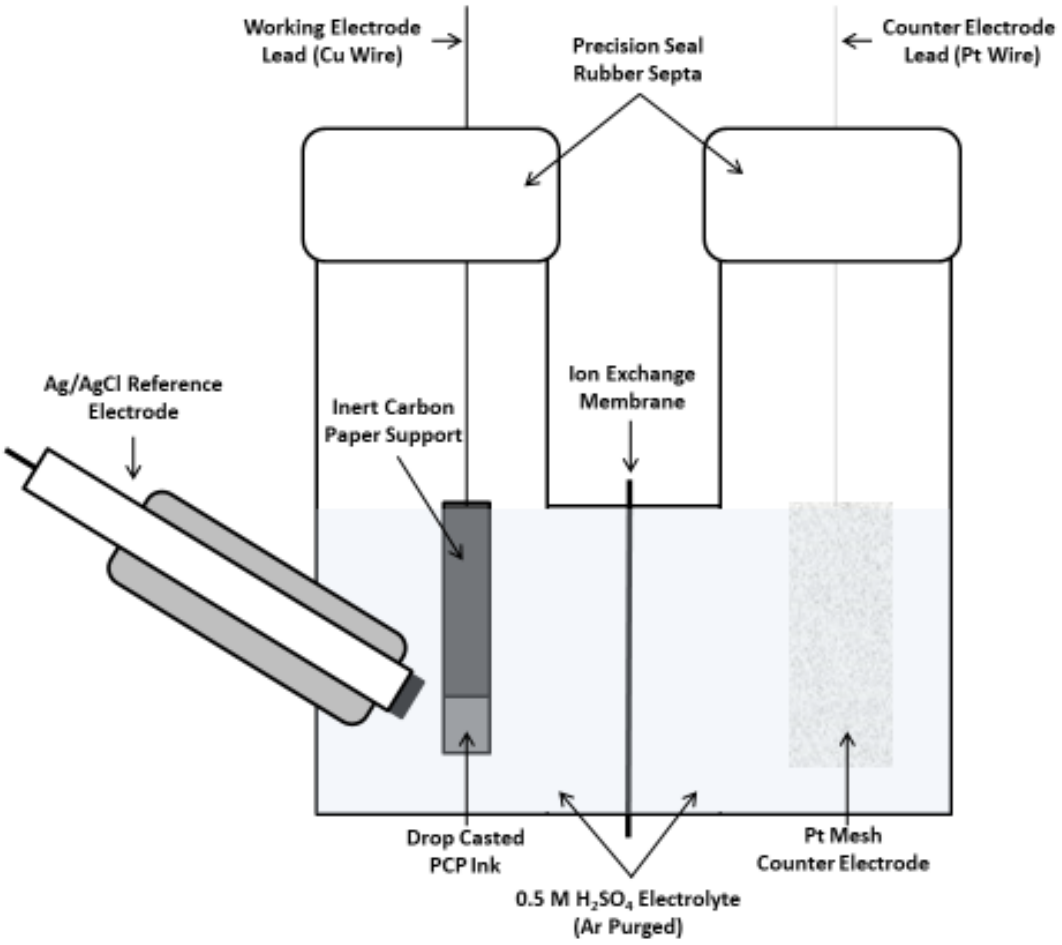

Figure S2. Schematic representation of the H-shaped three-electrode configuration that was implemented in all electrochemical experiments.

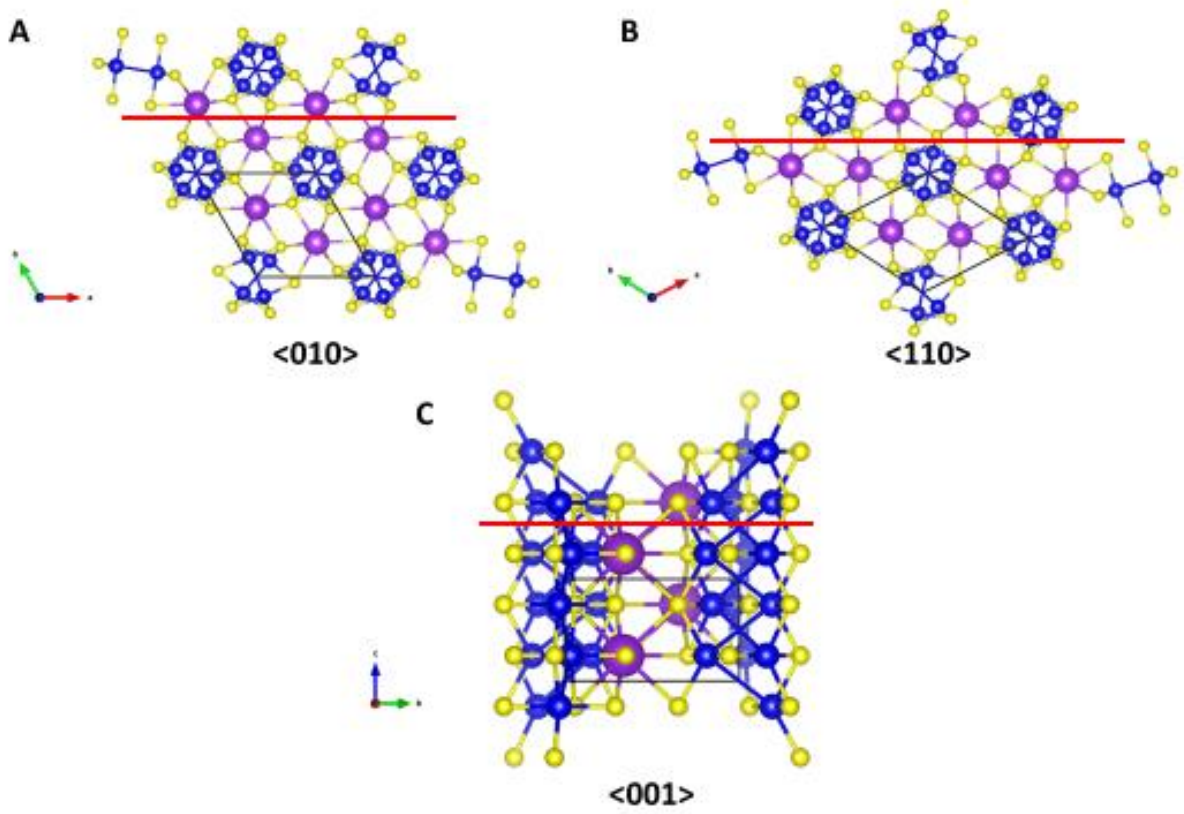

Figure S3. Crystal structure representations for each surface for which computational free energies were determined, illustrating an increasing number of broken bonds in moving from **(A)** <010>, to **(B)** <110>, and finally to **(C)** <001>. In each case, the compass shows that the unit cell is oriented such that the lattice plane is parallel to the viewing perspective.

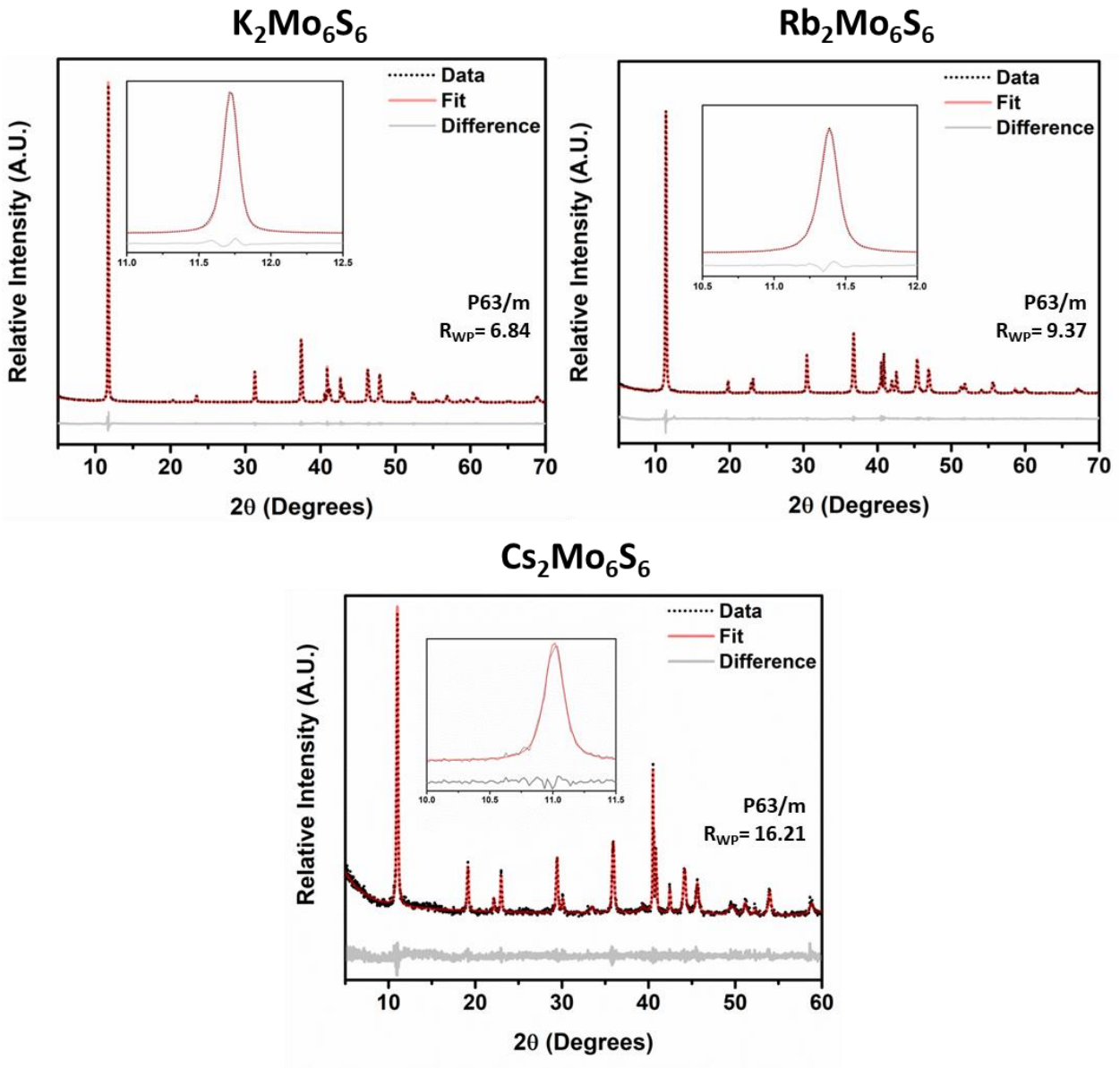

Figure S4. PXRD patterns used for Pawley refinement (black dots), along with their calculated patterns (red line) and the difference curve (grey line) for all three PCPs studied. Insets in each case contain the characteristic (010) peak of the PCP crystal system illustrating a relatively large degree of asymmetry, consistent with many low-angle diffraction peaks.

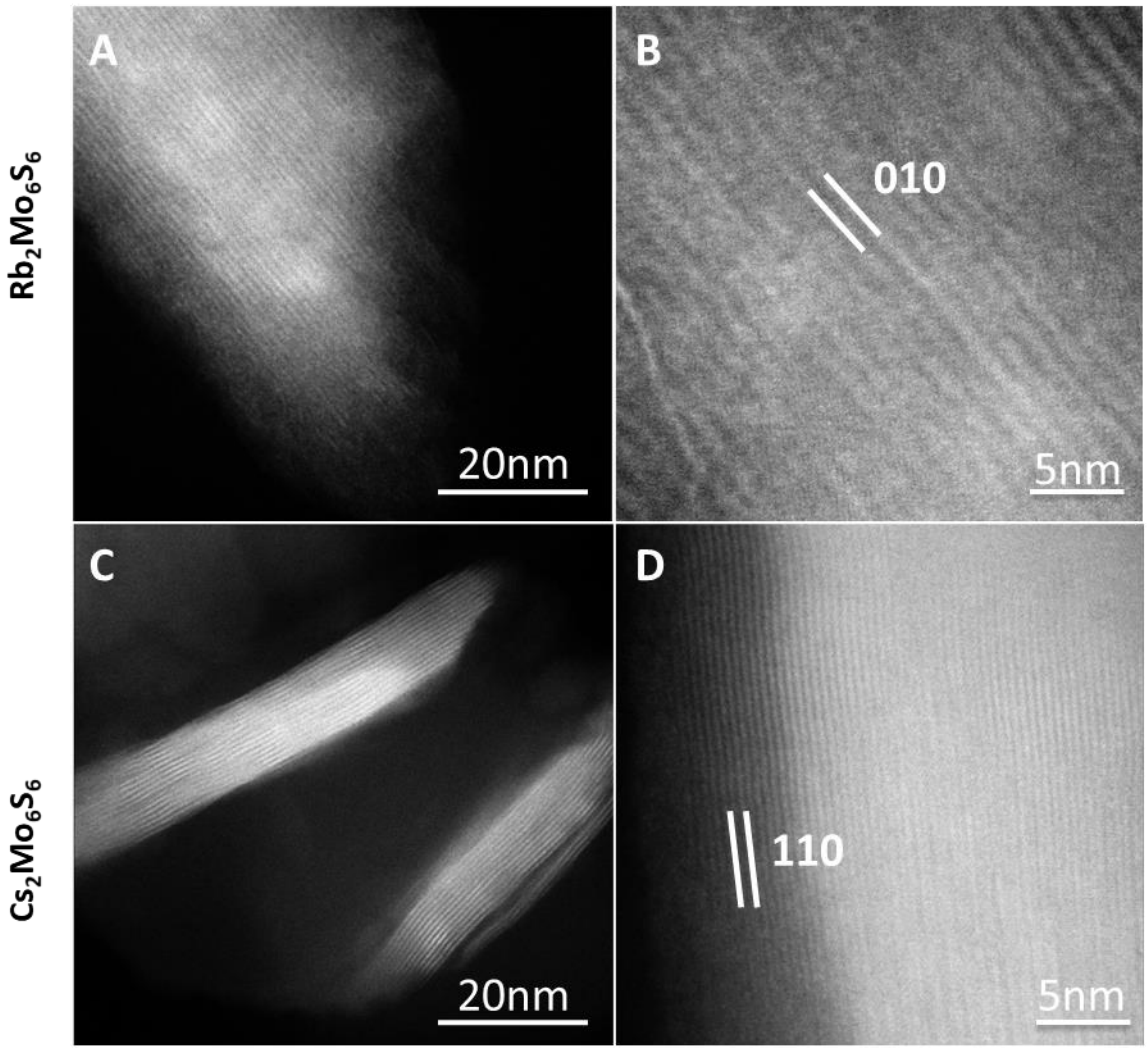

Figure S5. Lattice-resolved TEM images for Rb-PCP and Cs-PCP that illustrate the (010) and (110) directions, respectively. K-PCP was omitted owing to the thickness of K-PCP rods preventing required levels of transmission for lattice imaging.

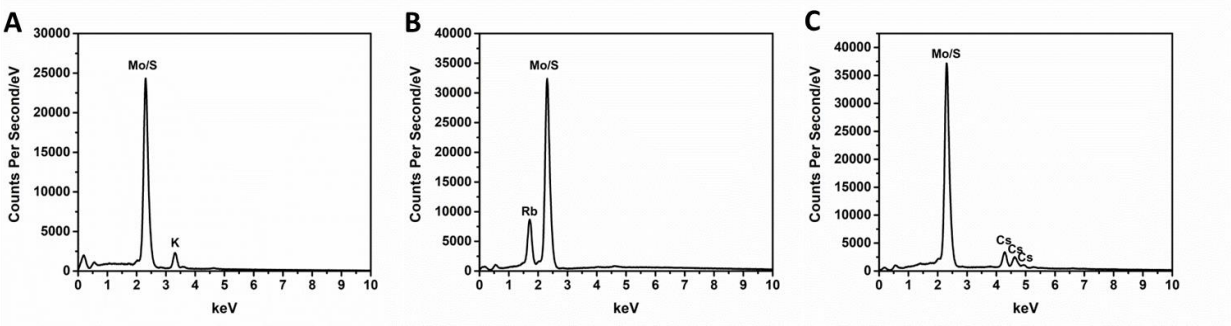

Figure S6. EDX spectra for **(A)** K-PCP, **(B)** Rb-PCP, and **(C)** Cs-PCP, illustrating no bulk elemental impurities for the rods synthesized here, and no significant evidence of bulk oxidation as might be expected from a nano-scale chalcogenide. Average alkali metal atomic percent compositions for each M_2-PCP are listed and are in good agreement with expected values within the error of EDX quantification, although Mo/S composition is omitted owing to strong overlap between Mo Lα1 and S Kα1 lines which convolutes their quantification.

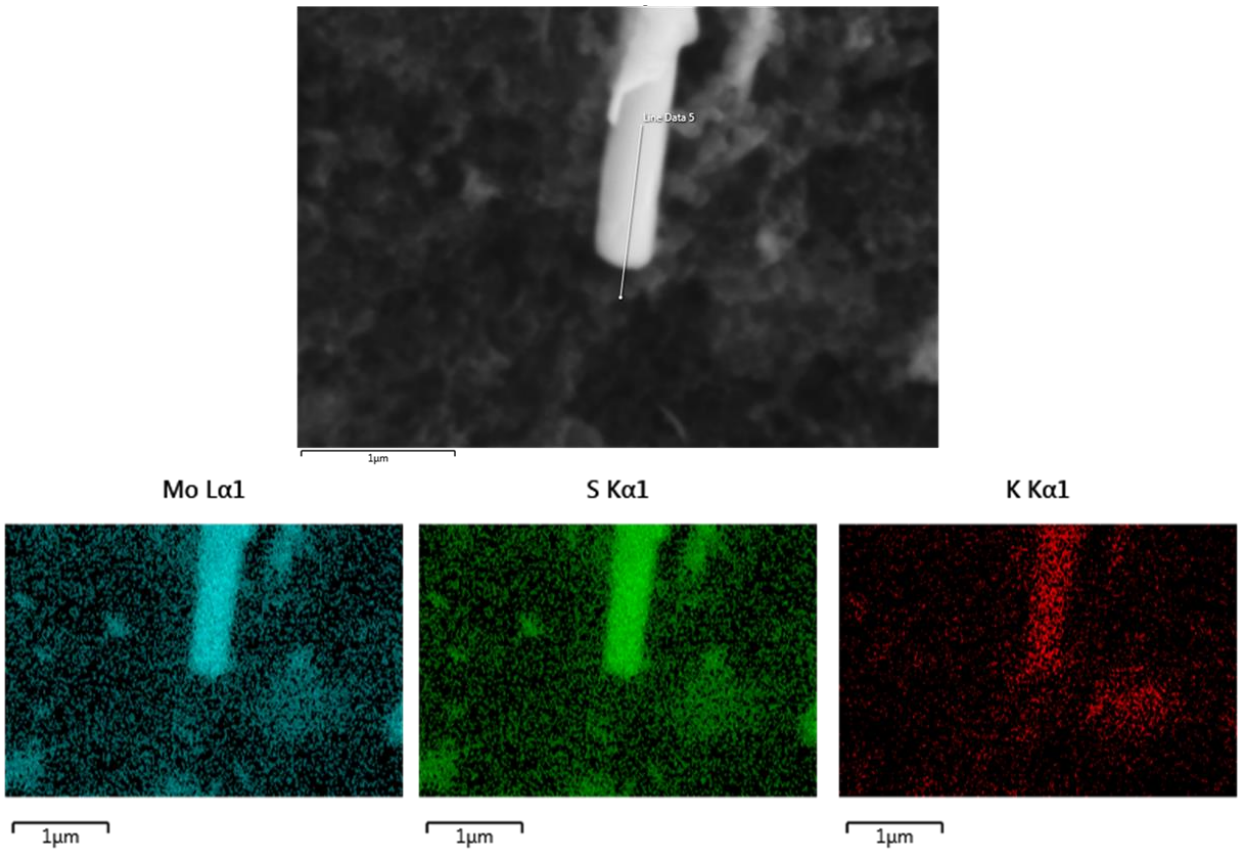

Figure S7. Result of EDX mapping of an individual K-PCP nanorod, performed with an accelerating voltage of 10keV and beam current of 3.2nA, illustrating uniform elemental distribution throughout the entirety of the rod. The corresponding line scan is shown in **Figure S8**.

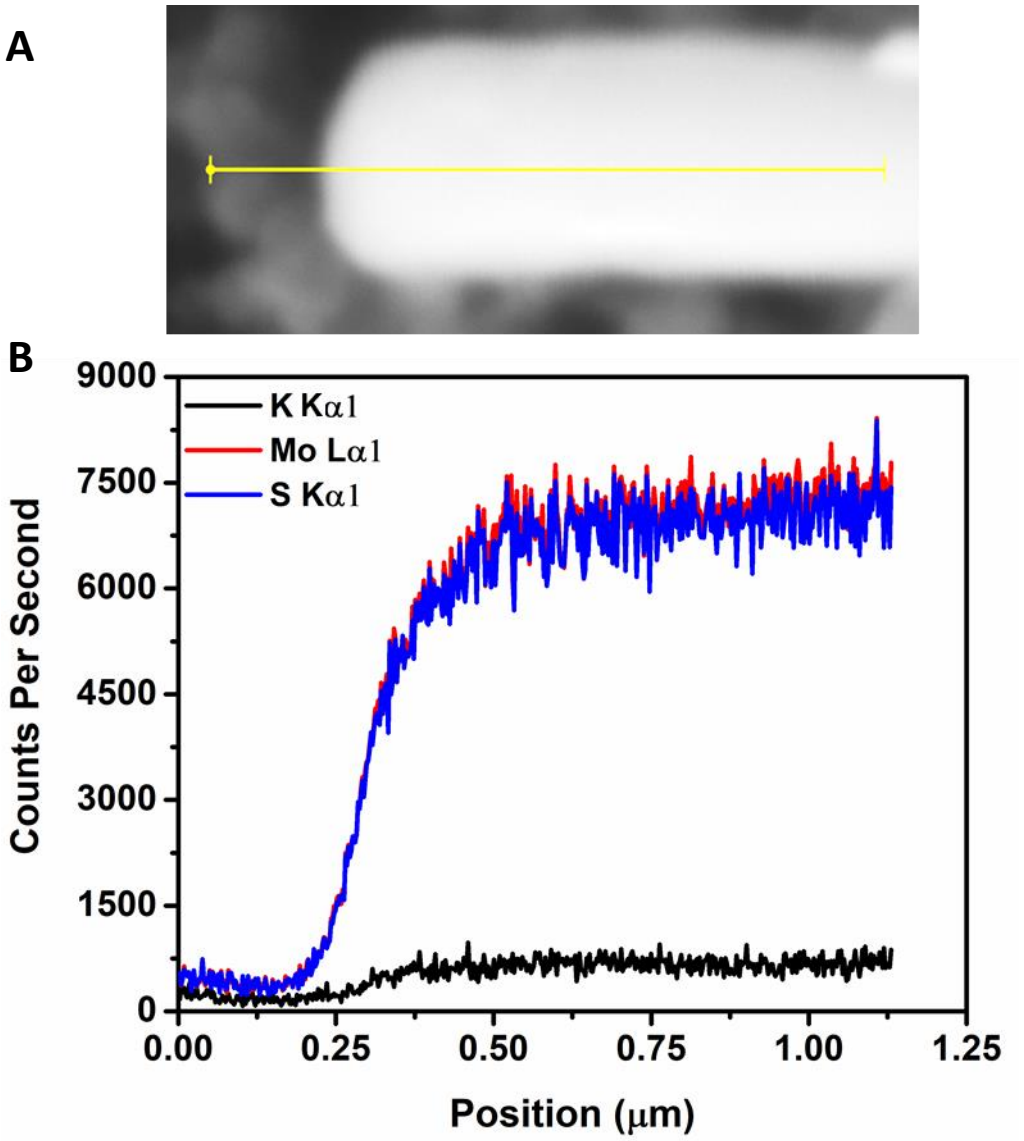

Figure S8. EDX line scan for the isolated K-PCP nanorod shown in **Figure S7**. Constituent element signals scale with sample thickness under the electron beam, and is uniform along the length of the rod. The scan position represented by a yellow line in the corresponding SEM **(A)** has been aligned to scale with the position axis in **(B).**

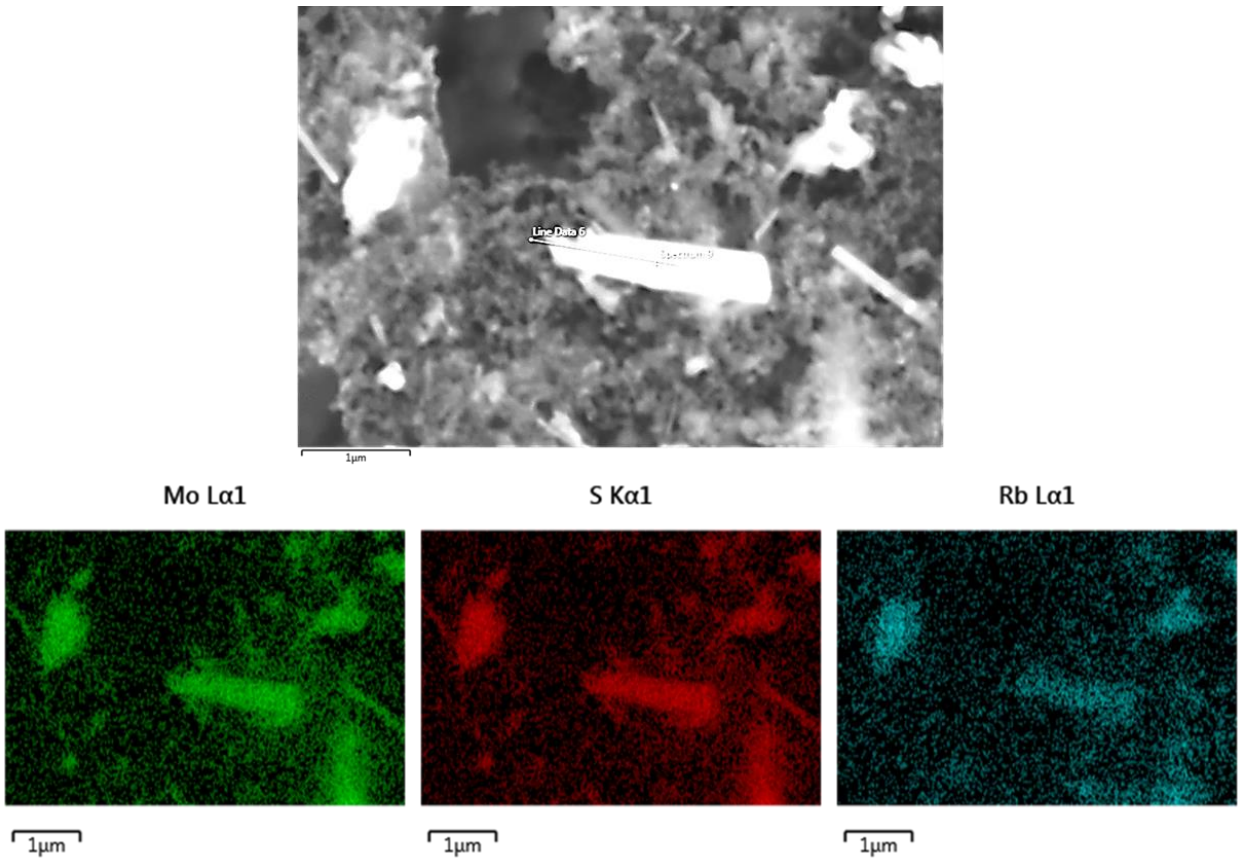

Figure S9. Result of EDX mapping of an individual Rb-PCP nanorod, performed with an accelerating voltage of 10keV and beam current of 3.2nA, illustrating uniform elemental distribution throughout the entirety of the rod. The corresponding line scan is shown in **Figure S10**.

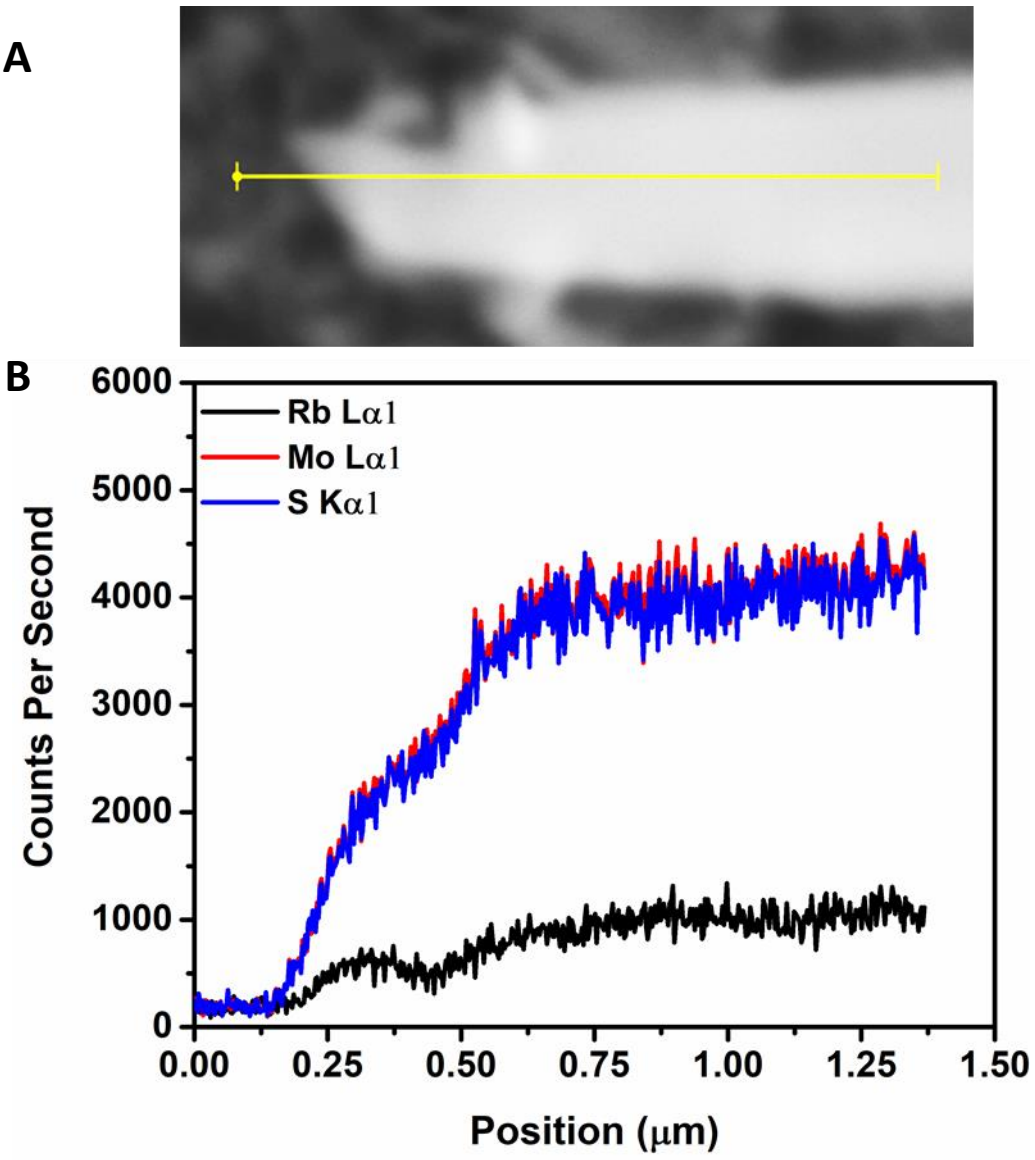

Figure S10. EDX line scan for the isolated Rb-PCP nanorod shown in **Figure S9**. Constituent element signals scale with sample thickness under the electron beam, and is uniform along the length of the rod. The scan position represented by a yellow line in the corresponding SEM **(A)** has been aligned to scale with the position axis in **(B).**

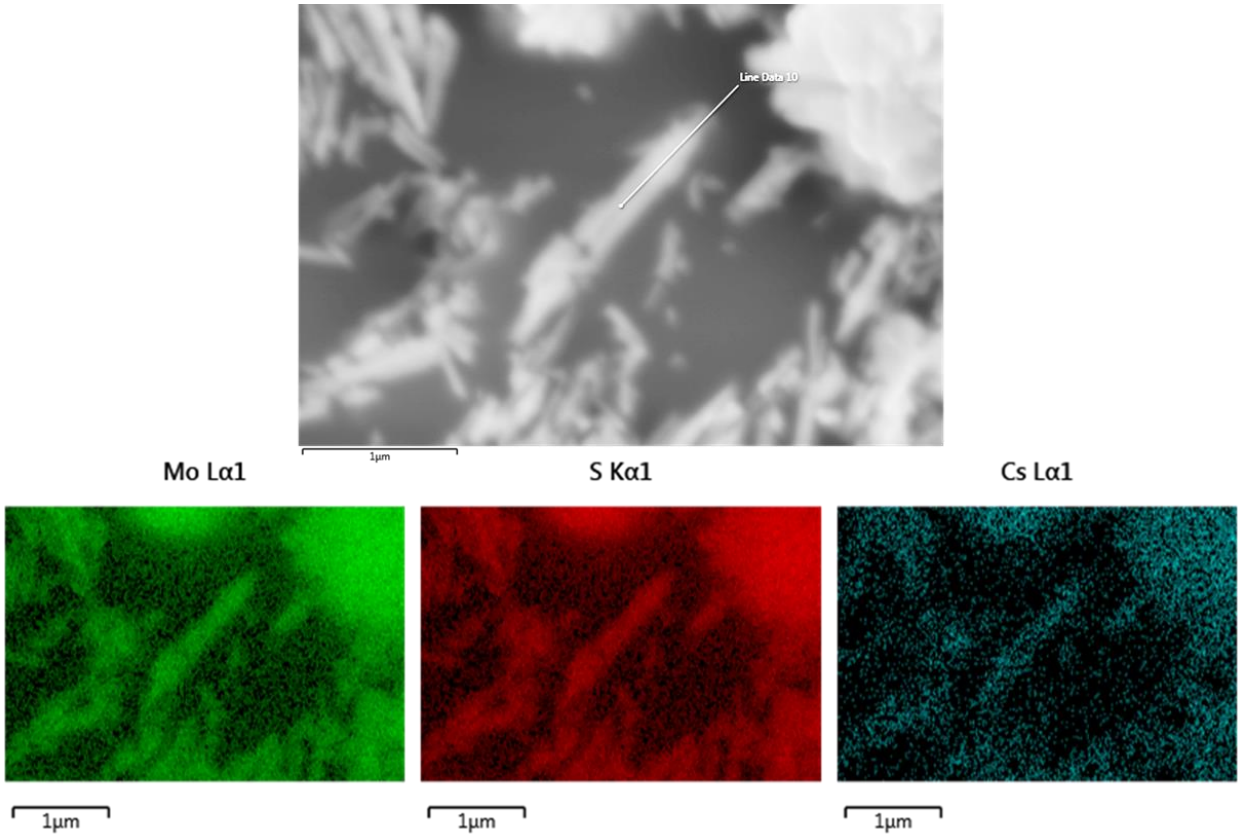

Figure S11. Result of EDX mapping of an individual Cs-PCP nanorod, performed with an accelerating voltage of 10keV and beam current of 3.2nA, illustrating uniform elemental distribution throughout the entirety of the rod. The corresponding line scan is shown in **Figure S12**.

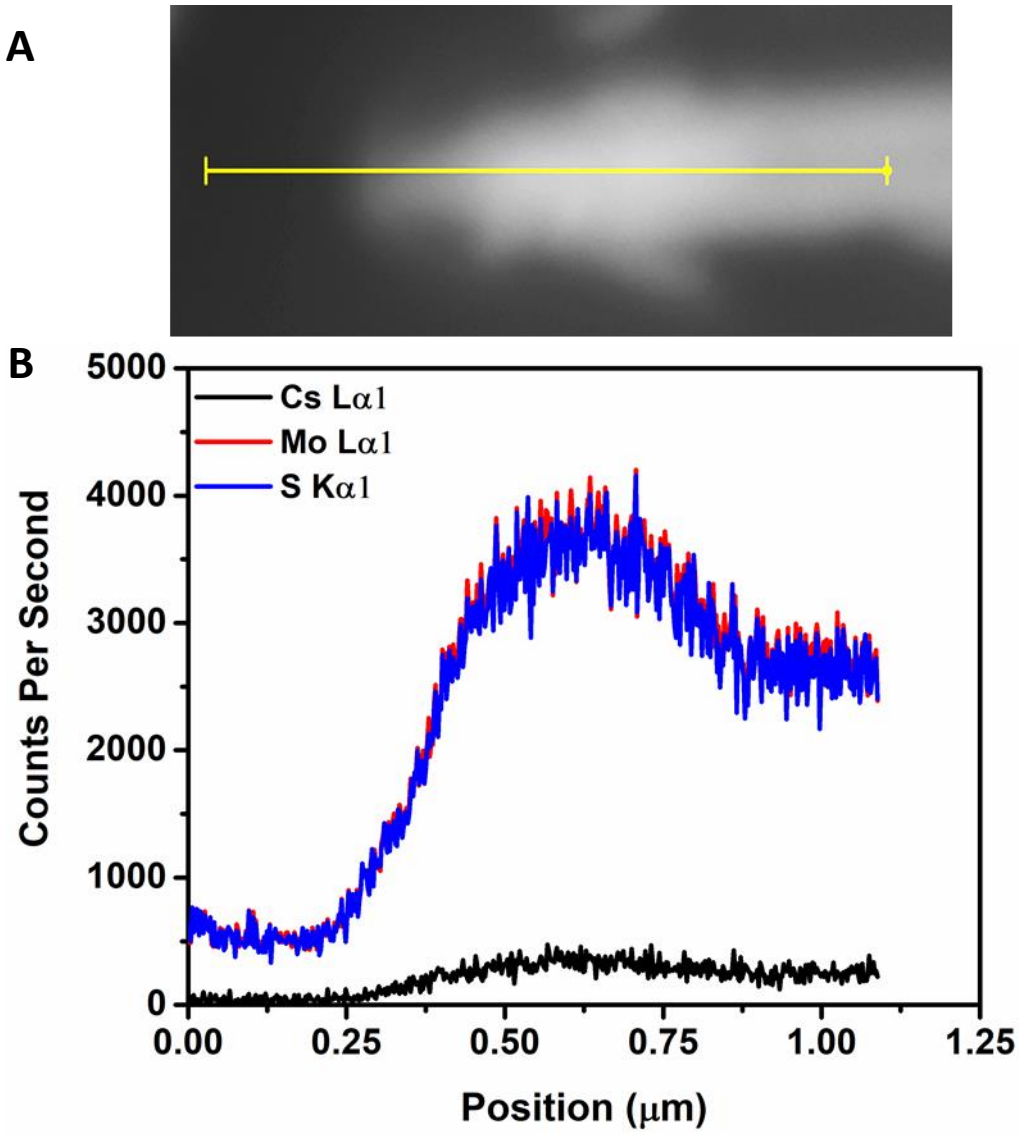

Figure S12. EDX line scan for the isolated Cs-PCP nanorod shown in **Figure S11**. Constituent element signals scale together with sample thickness under the electron beam. Intensity of each component decreases from ~0.6μm onward owing to decreased thickness of the rod. The scan position represented by a yellow line in the corresponding SEM **(A)** has been aligned to scale with the position axis in **(B).**

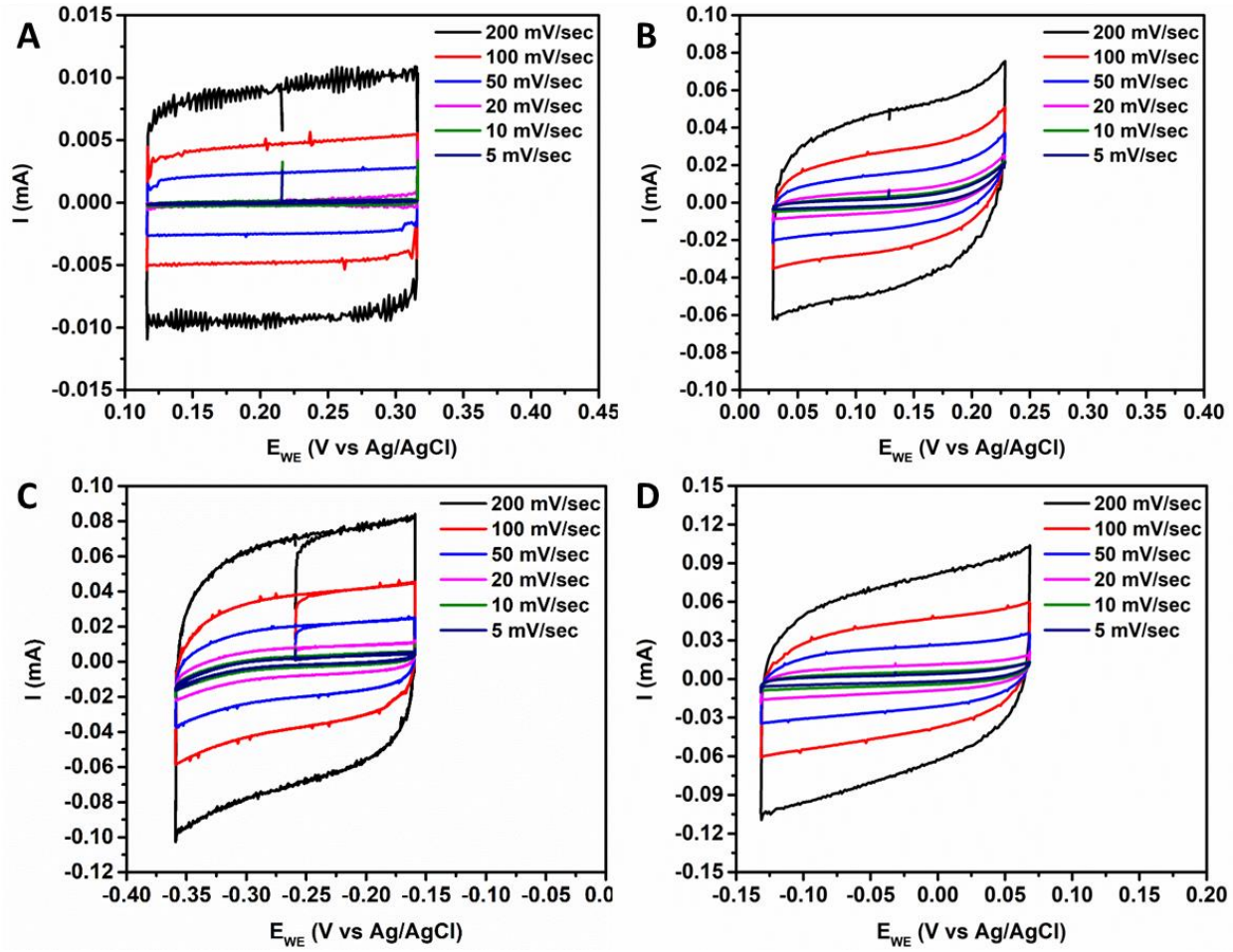

Figure S13. Scan-rate dependent cyclic voltamograms performed in 0.5M H_2SO_4 for **(A)** a blank ink without PCP, **(B)** K-PCP, **(C)** Rb-PCP, and **(D)** Cs-PCP. Voltammograms were collected in a region +/- 0.1V from each electrode's open circuit potential, as this region is generally non-Faradaic and therefore measured currents accurately represent purely capacitive charging. To ensure reliable statistics, CVs similar to the ones shown here were repeated for at least 6 electrodes of each ink.

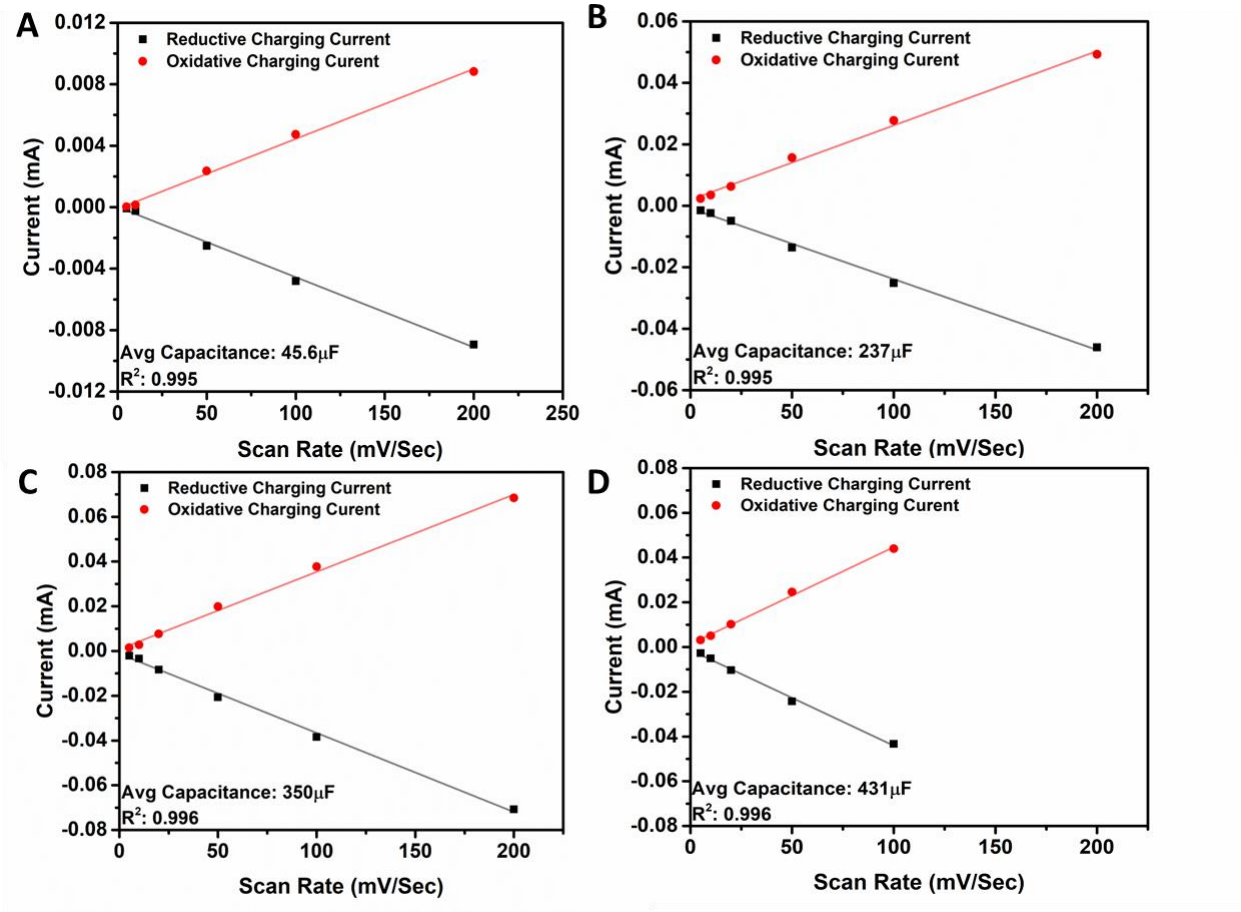

Figure S14. Examples of oxidative and reductive charging currents for **(A)** PCP-free blank ink, **(B)** K-PCP, **(C)** Rb-PCP, and **(D)** Cs-PCP. Capacitance is taken as the average of the absolute value for both positive and negative slopes in each case. In some experiments, 200mV/sec scans resulted in a large amount of noise, and are excluded on a case by case basis. Average capacitance values shown here represent the values for these specific scans, and are not the average values following replicated scans as reported in the main text.

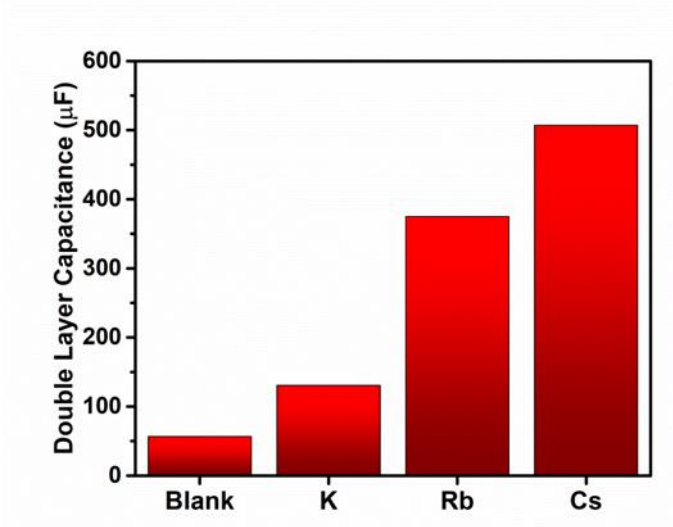

Figure S15. Double layer capacitance for each of the inks studied herein, taken as the average slope of all repeated current versus scan-rate plots.

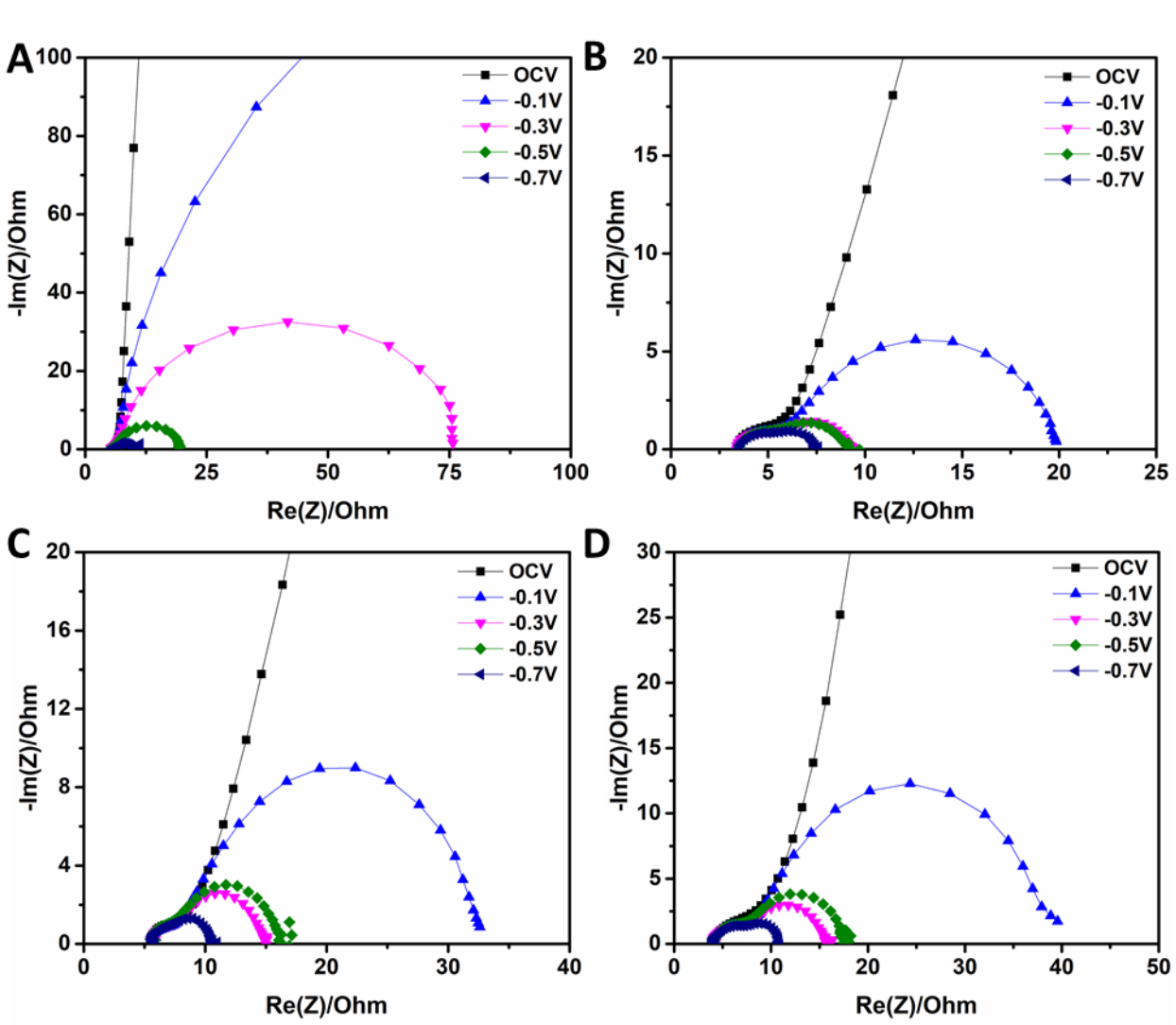

Figure S16. Examples of Nyquist plots for **(A)** PCP-free blank ink, **(B)** K-PCP, **(C)** Rb-PCP, and **(D)** Cs-PCP that were used to determine interfacial charge transfer resistance. Using a Randle circuit, resistance to charge transfer is taken as the difference between extrapolated x-intercepts at low AC frequency (right side) and at high frequency (left side).

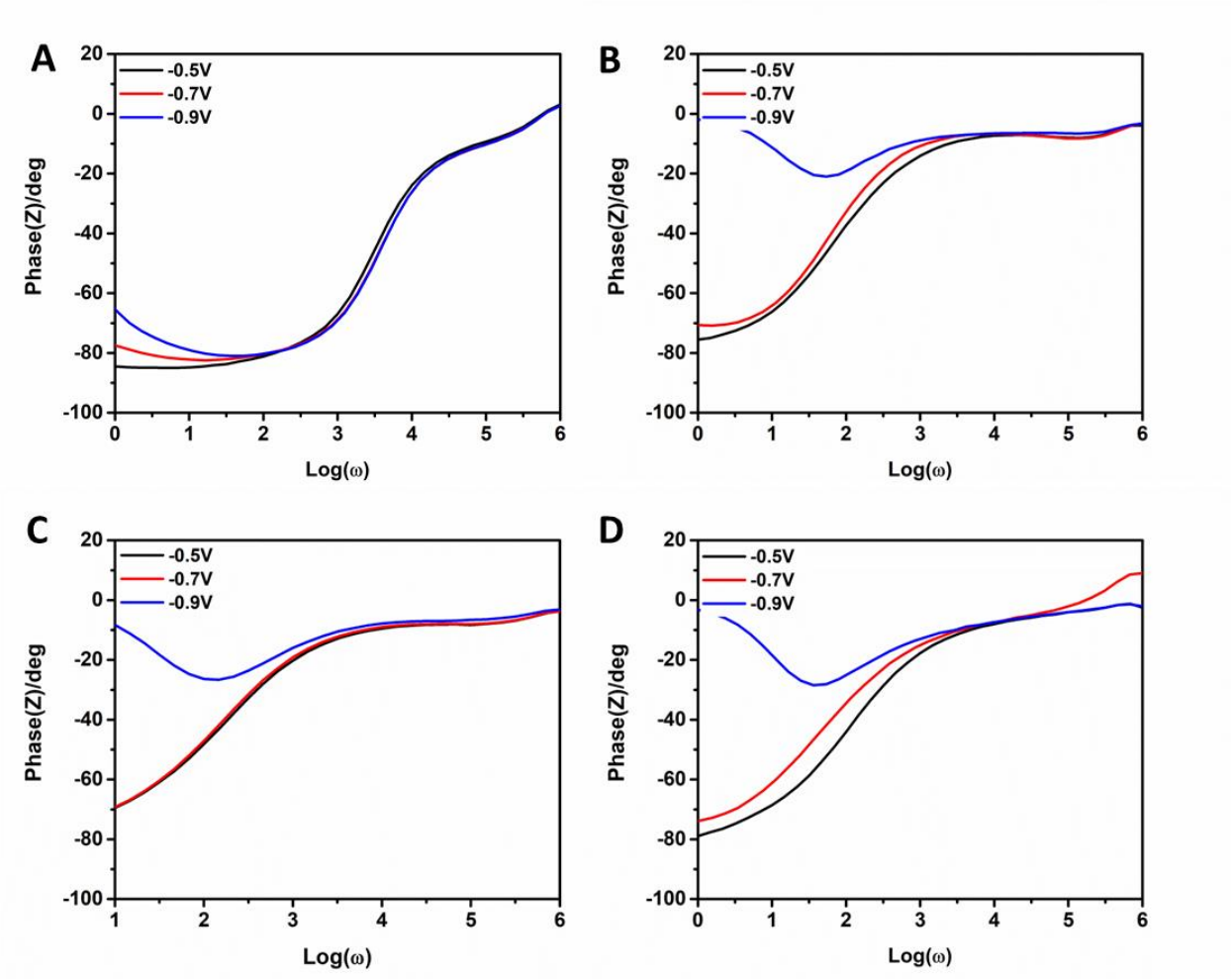

Figure S17. Phase angle response during potential-dependent EIS experiments for **(A)** PCP-free blank ink, **(B)** K-PCP, **(C)** Rb-PCP, and **(D)** Cs-PCP where ω is the AC bias frequency.

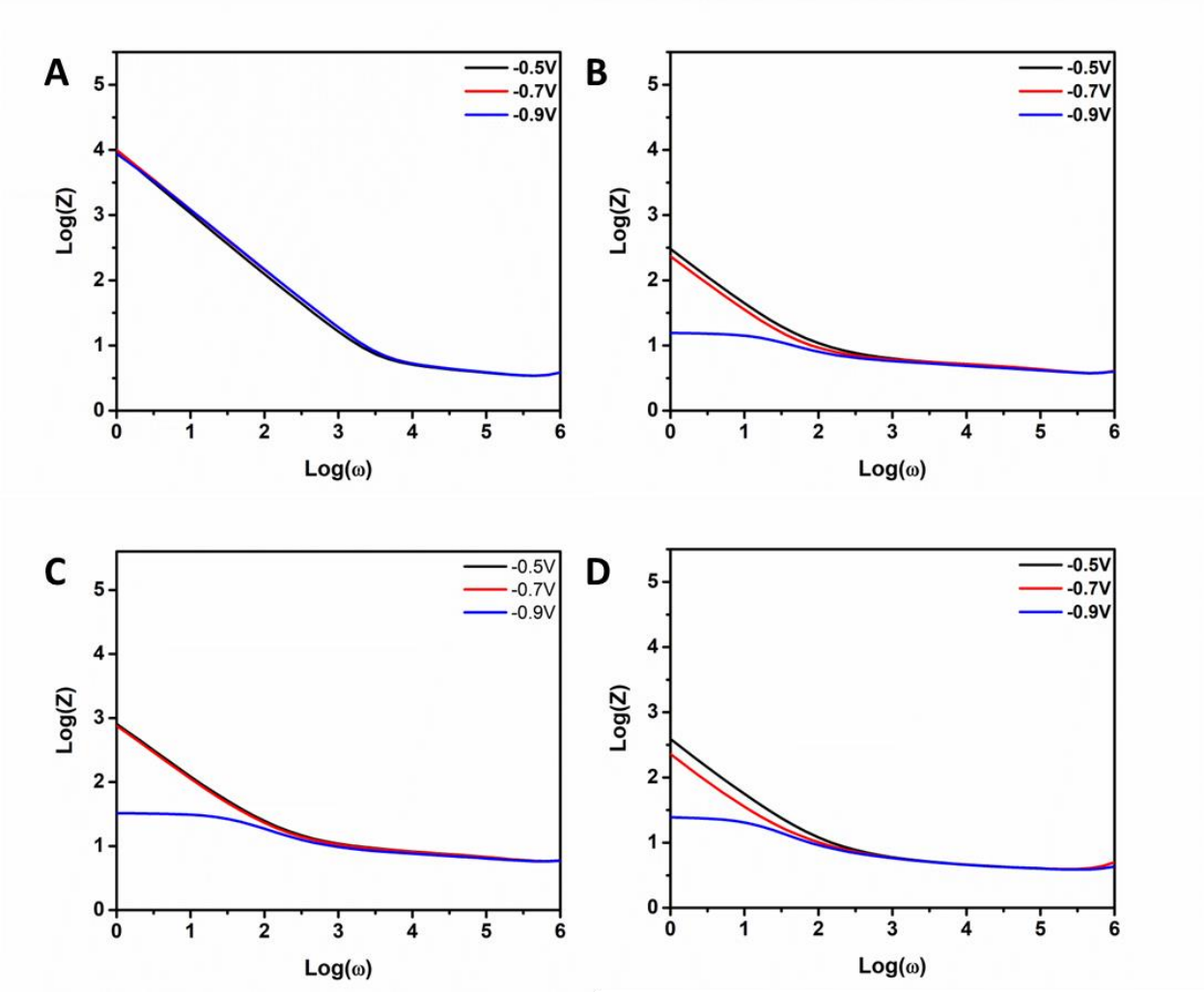

Figure S18. Impedance modulus response during potential-dependent EIS experiments for **(A)** PCP-free blank ink, **(B)** K-PCP, **(C)** Rb-PCP, and **(D)** Cs-PCP where ω is the AC bias frequency. Low frequency regions in all cases exhibit potential-dependent diffusion control, evidenced by the ~45 degree response of the impedance modulus.

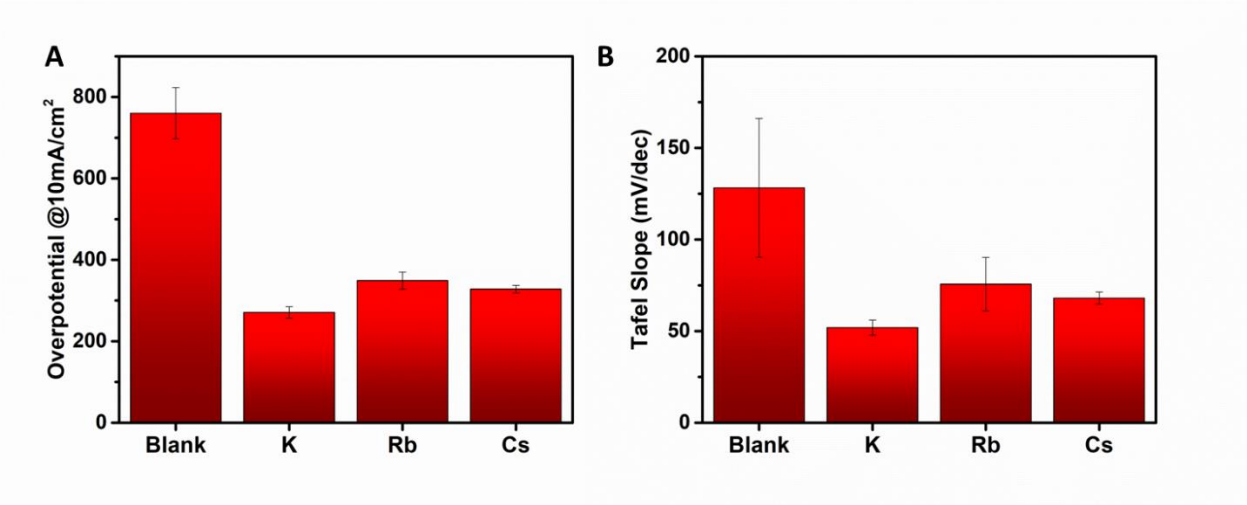

Figure S19. (A) Average overpotential required to achieve a current density of 10mA/cm^2 for all four inks, and **(B)** Average Tafel slope calculated for all four inks. In both figures, error bars represent a single standard deviation.

Table S1. Results of computational surface energy modeling for K_2-PCP <010>, <110>, and <001> surfaces.

Facet	Surface energy (eV/ Formula Unit)
<010>	0.37
<110>	0.93
<001>	4.19

Table S2. Compiled lattice parameters extracted via Pawley refinement for $M_2Mo_6S_6$, compared with literature values

Parameter	This Work	Literature	%Difference
$K_2Mo_6S_6$			
a	8.7346	8.7204	0.16%
b	8.7346	8.7204	0.16%
c	4.4136	4.4076	0.14%
α	90	90	0.00%
β	90	90	0.00%
γ	120	120	0.00%
Cell Volume	291.61	290.27	0.46%
$Rb_2Mo_6S_6$			
a	8.9553	8.9589	-0.04%
b	8.9553	8.9589	-0.04%
c	4.4046	4.4114	-0.15%
α	90	90	0.00%
β	90	90	0.00%
γ	120	120	0.00%
Cell Volume	305.912	306.63	-0.23%
$Cs_2Mo_6S_6$			
a	9.2518	9.269	-0.19%
b	9.2518	9.269	-0.19%
c	4.4114	4.419	-0.17%
α	90	90	0.00%
β	90	90	0.00%
γ	120	120	0.00%
Cell Volume	327.008	328.86	-0.56%